A novel electron source for a compact x-ray tube for microbeam radiotherapy with very high dose rates

Christoph Matejcek[2,4,*], Johanna Winter[1,2,3], Kurt Aulenbacher[4,5,6], Anton Dimroth[7,8], Ghaleb Natour[7,8], and Stefan Bartzsch[1,2]

[1]Helmholtz Zentrum München GmbH, German Research Center for Environmental Health, Institute of Radiation Medicine, Neuherberg, Germany

[2]Technical University of Munich, School of Medicine and Klinikum rechts der Isar, Department of Radiation Oncology, Munich, Germany

[3]Technical University of Munich, Physics Department, Garching, Germany

[4]Johannes Gutenberg-Universität Mainz, Institut für Kernphysik, Mainz, Germany

[5]GSI Helmholtzzentrum für Schwerionenforschung, Darmstadt, Germany

[6]Helmholtz-Institut Mainz, Germany

[7]Forschungszentrum Jülich GmbH, Central Institute for Engineering, Electronics and Analytics (ZEA), Jülich, Germany

[8]RWTH Aachen University, Faculty of Mechanical Engineering, Aachen, Germany

[*]Corresponding author: matejcek@uni-mainz.de, Johannes Gutenberg-Universität Mainz, Institut für Kernphysik, Johann-Joachim-Becher-Weg 45, 55128 Mainz, Germany

March 2022

Highlights:

- Line-focus x-ray tubes are suitable for clinical microbeam radiation therapy (MRT) with very high dose rates.
- With tracking simulations, a suitable setup for an electron source and beamline was found.
- Additional electrostatic simulations ensure fields sufficiently low to avoid a field breakdown.
- Thermal simulations identified mechanical displacements after heating up the cathode, which must be compensated.

Abstract

Microbeam radiotherapy (MRT) is a novel concept in radiation oncology with arrays of alternating micrometer-wide high-dose peaks and low-dose valleys. Preclinical experiments have shown a lower normal tissue toxicity for MRT with similar tumor control rates compared to conventional radiotherapy. A promising candidate for the demanded compact radiation source is the line-focus x-ray tube. Here, we present the setup of a prototype for an electron accelerator being able to provide a suitable x-ray beam for the tube.

Several beam dynamic calculations and simulations were performed concerning particle tracking, thermal and electrostatic properties of the electron source, resulting in a proper beamline, including the cathode, the pierce electrode (PE) and the focusing magnets. These parts are discussed separately.

The simulations showed that a rectangular cathode with a small width of 0.4 mm is mandatory. To quickly shut down the electron beam, an additional voltage of $-600\,\mathrm{V}$ must be applied to the PE. Moreover, the electric field inside the vacuum chamber stays below $10\,\mathrm{MV\,m^{-1}}$ to minimize the risk of field emission. The thermal simulation validates a small displacement of 0.1 mm of the heated cathode with respect to the PE, which must be considered during manufacturing of the cathode-PE assembly.

The simulations lead to an adequate choice of cathode, electrodes and beamline to achieve the required focal spot of $0.05 \times 20\,\mathrm{mm^2}$ with a beam current of 0.3 A and an electron energy of 300 keV. With this setup first MRT experiments with high dose rates up to $10\,\mathrm{Gy\,s^{-1}}$ can be executed.

Keywords:

- Microbeam radiation therapy
- Line-focus x-ray tube
- Electron source
- Tracking simulation
- Electrostatic simulation
- Thermal simulation

1 Introduction

Microbeam radiotherapy (MRT) [1], which is a preclinical concept in radiation oncology, demonstrated superior normal tissue sparing at similar tumor control rates compared to conventional radiotherapy [2, 3]. It has the potential of treating patients with aggressive tumors in radiation sensitive tissues, which have so far dismal prognosis. MRT uses spatially modulated treatment fields with alternating micrometer-wide high-dose peaks and low-dose valleys [4]. Regardless of the used particles or radiation, the use of spatially fractionated beams improves the ability of normal tissues to resist high doses [5]. The planar and quasi-parallel kilovoltage x-ray beams of MRT have a width of 25–100 µm and unconventionally high doses of several 100 Gy. In addition, a high dose rate of several $100\,\mathrm{Gy\,s^{-1}}$ at the target is beneficial to prevent blurring of the microbeam pattern caused by organ motion [6]. Furthermore, the peak-to-valley dose ratio (PVDR) must be high [6] and the minimization of the penumbras is beneficial.

This demands for a radiation source with a focal spot in one dimension smaller than an individual beam and high dose rates. A promising concept for a compact clinical source is the line-focus x-ray tube (LFxT) [7, 8]. This x-ray tube uses a strongly eccentric, high current electron beam to produce the x-rays at a rapidly rotating target. The extremely thin focal spot in combination with the fast rotating target result in a change of the physical heating process of the target [7], which allows providing the required high beam current without melting the target material. Monte Carlo simulations showed that the electrons need to be accelerated to energies between 300 and 600 keV to produce photons with mean energies of 100–150 keV at a tungsten target.

Suggested requirements for an LFxT utilized for a clinical application are the following [7]: a dose rate of $180\,\mathrm{Gy\,s^{-1}}$ (50 cm from the focal spot), an acceleration voltage of 600 kV, an electron current of 2.5 A, leading to a power of 1.5 MW, and a focal spot size of $0.05 \times 20\,\mathrm{mm^2}$. It must be mentioned that orthovoltage radiation has steeper dose profiles and may therefore have disadvantages for the

treatment of deep tumours. However, in a recent work we showed that reasonable dose distributions, which are comparable to conventional treatments, can be achieved e.g. for lung and brain tumours [9]. Hence, the disadvantage of steeper depth dose curves may be outweighted by the spatial fractionation which needs a clinical validation. For a demonstration of the feasibility, to address difficulties, and for preclinical MRT research, a prototype of the LFxT is under construction. This prototype uses a lower voltage of 300 kV and a lower current of 0.3 A resulting in a beam power of 90 kW. This power is an order of magnitude lower than for the clinical device, however lies at the upper edge of common x-ray tube beam powers [10].

In this study, we present the investigations of a feasible electron source for the prototype of a clinical LFxT. Achieving a very small focal spot requires a low emittance, which is a figure of merit for the dimension and divergence of the electron beam. In combination with the demanded high electron beam current, realizing a small emittance is challenging because of a high space charge force inside the electron beam. The space charge force has nonlinear contributions leading to a growth of the emittance. The goal of the prototype is to realize a focal spot width of 50 µm in one dimension with an electron beam current of 0.3 A. In the other dimension, the size of the focal spot is determined to stay between 20 and 30 mm. On the one hand, a smaller spot creates a higher temperature of the target and risks substantial damage. On the other hand, a larger spot has the drawback of creating larger penumbras in the x-ray beam. Furthermore, the prototype will use an accelerating voltage of 300 kV. The relatively low electron energy combined with a high beam current is a demanding issue and asks for a short acceleration distance. Nevertheless, the energy is sufficiently high to cause critical field emission and high voltage breakdown, which in the worst case damage the device. This is in conflict with a short acceleration distance and a compact device. Tracking, static electric and thermal simulations were performed to find a suitable electron gun and beamline. We show simulation results and the final setup of the source and beamline.

2 Material and Methods

The LFxT demands an eccentric focal spot with an extremely small size in one dimension at a high beam current to deliver a highly brilliant x-ray beam with a high dose rate. Although the small focus must be realized only in one direction, combining small beam sizes with high beam currents is challenging for an electron accelerator. The electron accelerator consists of a cathode for extraction of the electrons, an anode on acceleration potential and a focusing element. Additionally, a Pierce electrode (PE) around the cathode is necessary to focus the beam directly after extraction. With the help of beam dynamic calculations and tracking simulations the required beam parameters can be determined and the properties and the arrangement of the devices can be defined. In the following, the dimension with the small focus size is the y-/vertical direction and the beam axis is the z-/longitudinal direction.

2.1 Beam dynamics

Beam dynamic calculations provide a first choice of beam parameters needed to achieve a $0.05 \times 20\,\mathrm{mm}^2$ focal spot, which is important for the selection of the cathode, magnet and simulation parameters. The transverse beam size a, meaning either x or y, along the beamline s can be expressed as

$$a(s)^2 = \epsilon_a \left(\beta_0 + \frac{s^2}{\beta_0} \right) \text{ with } a(0)^2 = \epsilon_a \beta_0. \tag{1}$$

Here, β_0 is one of the Twiss-parameters. The motion of the particles are oscillations around the beam orbit whose amplitude and phase depend on the position along the orbit. This motion can be described by an ellipse in the transverse phase space along the orbit. The parameters of the ellipse are the Twiss-parameters (see [11]). The quantity ϵ_a indicates the normalised rms-emittance (rms: root mean square). In general, beam parameters are expressed as rms-parameter. For a homogeneous beam, the overall beam size is four times the rms-value. The emittance is defined as

$$\epsilon_a = \gamma\beta\sqrt{\langle a^2 \rangle \langle a'^2 \rangle - \langle aa' \rangle^2}, \tag{2}$$

where β is the relativistic velocity and γ denotes the Lorentz factor. The emittance is a measure of the beam geometry, meaning its size and divergence, and limits the minimal reachable focus size. Equation 1 reveals that for a small focus spot a small emittance is important.

To achieve such a small focus spot, strong focusing is required. We chose a focusing length of $s_\mathrm{f} = 10\,\mathrm{cm}$ to provide space for the magnet and vacuum chamber with its cooling system. A smaller focusing length increases the heat introduced by secondary electrons, which are produced at the target, to the vacuum chamber, because more secondary electrons per area will hit the chamber wall. Furthermore, a stronger focusing needs a higher magnetic field, the non-linear components of which lead to larger emittance growth limiting the focus size. The presence of non-linear components has also an influence on the initial beam dimension. The non-linear field components are stronger at a larger distance from the beam axis. As a consequence, large beams suffer more from this components. To avoid emittance growth of several percent, the initial beam dimension in front of the quadrupole should not exceed $y_\mathrm{i} = 1.5\,\mathrm{mm}$ [12]. Taking this under consideration and using equation 1 defines an upper limit for the emittance of $\epsilon_y = 0.19\,\mathrm{mm\,mrad}$ for a focal rms beam size of $y_\mathrm{f} = 12.5\,\mu\mathrm{m}$. So far, the self field of the beam, meaning the electromagnetic field introduced by its charge, was neglected. Unfortunately, these fields as the space charge forces scale with $\frac{1}{\beta^2\gamma^3}$ and need to be taken into account for low energies. The K-V-equations (Kapchinskij-Vladimirskij), which can be derived from the equations of motion, describe the rms-envelope of the beam under consideration of space charge (see also [12, 13]). The calculations considering the space charge define a lower limit of the emittance than mentioned before, namely $\epsilon_y = 0.17\,\mathrm{mm\,mrad}$ caused by the additional repulsive space charge field of the beam. With this value, the diameter in the x-dimension is around 30 mm. The following goal was to construct an electron source and beamline that provides an emittance of $\epsilon_y = 0.17\,\mathrm{mm\,mrad}$ and a beam dimension of $y_\mathrm{i} = 1.5\,\mathrm{mm}$ in front of the quadrupole magnet.

Parameter	Range
Angle of PE	10–23°
Temperature of cathode	1243–1456 K
y_{cath}	0.1–1 mm
x_{cath}	5–22 mm
Distance anode and cathode	51–67 mm
Excitation current quadrupole 1	0–0.7 A
Excitation current quadrupole 2	0.7–1.4 A

Table 1: Simulated ranges of selected parameters of the electron beam.

2.2 Tracking simulations

To achieve more realistic results and to be able to implement the complex beamline components, tracking simulations were needed. The simulations of the electron source and beamline were done with Computer Simulation Technology (CST, [14]). To achieve a short simulation time, only relevant parts were included in the simulation, meaning the cathode, PE, anode and vacuum. The cathode, PE and anode structures were modelled with variable parameters of the sizes, distances, angles and the temperature. The position and field strength of the used magnets were additional variable quantities. The magnetic fields were calculated in a separate, dedicated simulation with CST and imported into the tracking simulation. In an iterative process, the parameters were optimised to achieve the aimed-at focus size and beam current. In table 1, selected parameters and the simulated ranges are listed.

2.3 Electrostatic simulations

Furthermore, CST is also capable of solving static electromagnetic problems. The results presented in [15] show that field emission can occur at electric fields $E_{\mathrm{break}} > 10\,\mathrm{MV\,m^{-1}}$, whereas in [16] the field strength for a breakdown lies above $20\,\mathrm{MV\,m^{-1}}$. The breakdown field strength depends on the geometry of

the electrodes. We decided to avoid fields above $10\,\mathrm{MV\,m^{-1}}$ to lower the risk of an electrical breakdown and damage at the components, especially at the high voltage (HV) insulator. Static electrical simulations were done to find a sufficient distance between cathode, anode and vacuum chamber. On the contrary, a short acceleration distance has a positive impact on the emittance growth caused by space charge. As mentioned, the self field of the electron beam strongly depends on the energy ($\frac{1}{\beta^2\gamma^3}$) and so does the emittance growth. Therefore, a fast acceleration, corresponding to a high gradient and a short acceleration distance, towards higher energy is beneficial. Additionally, the radius of the PE must be sufficiently large to avoid electric field strengths above $10\,\mathrm{MV\,m^{-1}}$. For the electrostatic simulations, the vacuum chamber and the electrodes were set to perfect electrical conductors, whereas the insulator consisting of Al_2O_3 had a relative permittivity of 10. The propylen-ethylen rubber of the HV-connector had a relative permittivity of 2.4.

2.4 Thermal simulations

The high temperature of the cathode $T_{\mathrm{cath}} \approx 1300\,\mathrm{K}$ needed to provide a beam current of 0.3 A causes thermal expansion of all parts of the cathode-PE assembly. Especially the large dimension of the PE can cause a large elongation due to an increase in temperature. A longitudinal displacement of cathode and PE, causing a deviation from the optimal position, changes the desired beam properties.

To investigate this issue, a thermal simulation of the final cathode design was conducted with Finite-Element-Analysis (FEA) in Ansys Mechanical [17]. The geometry model is shown in figure 1. The cathode consists of different materials with different thermal properties that are indicated in table 2. We chose a hexahedral mesh with an element size ranging from 0.25–2.5 mm. A steady-state heating power of 16W was applied to the tungsten cathode to reach the operation temperature $T_{\mathrm{cath}} \approx 1300\,\mathrm{K}$ of the cathode. All components within the PE have interacting thermal radiation conditions. At the back end of the

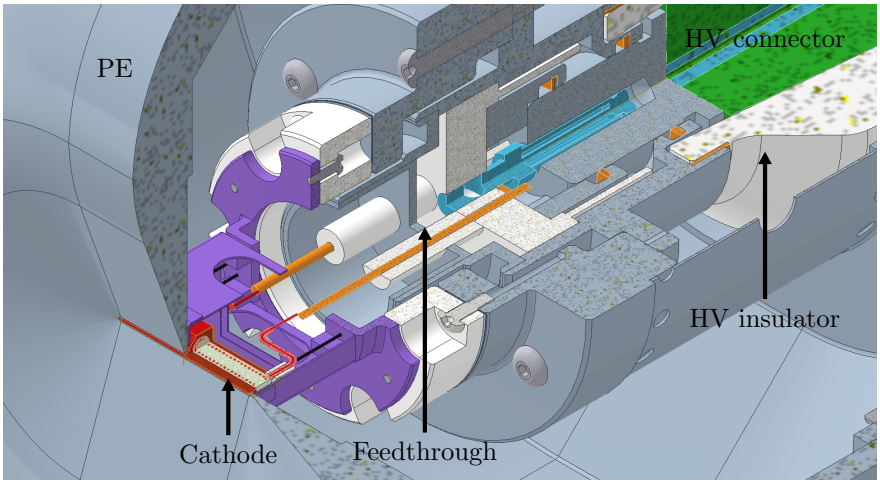

Figure 1: CAD model of the cathode; red: tungsten, steel blue: stainless steel AISI 316, purple: molybdenum, black: rhenium, white: Al_2O_3, turquoise: copper, green: polyvinyl chlorid (PVC), orange: nickel.

assembly (opposite site of the cathode), a constant room temperature works as a heat sink. Additionally, the flange at the end of the HV insulator has a non-moving constraint. After the thermal solution, the results were transferred to the mechanical module of Ansys workbench, to solve for the thermal expansions during the operation.

2.5 Cathode

There are several types of cathodes. The most commonly used cathodes in accelerator physics are thermionic and photo cathodes. Photo cathodes use a laser to extract the electrons and have the drawback that they consist of sensitive material. Therefore, they need ultra high vacuum and possess a short lifetime compared to thermionic cathodes. For the high currents demanded in this project and the expected vacuum of 1×10^{-7} mbar, thermionic cathodes are a better choice. There exists a variety of thermionic cathodes such as barium tungsten dispenser (BTD) or hexaboride cathodes. For the prototype, the BTD

Material	Thermal conductivity $\mathrm{W\,K^{-1}\,m^{-1}}$	Specific heat capacity $\mathrm{J\,K^{-1}\,kg^{-1}}$	Emissivity	Thermal expansion $10^{-6}\mathrm{K^{-1}}$
Al_2O_3	34.9	900	0.25 [18]	7.3
PVC	0.17	1	0.94	70
Stainless steel 316	15	500	0.57[19]	16
Tungsten	110	160	0.2-0.5	4.4
Copper	401	390	0.03	17
Rhenium	47.9	137	0.3	6.7
Molybdenum	100	250 - 290	0.11[19]	5.2
Nickel	85	418	0.12[19]	15

Table 2: Thermal properties of the used materials in the thermal simulations.

is sufficient and has the advantage to be more robust. However, for the clinical device the hexaboride cathodes should be considered as they are able to provide a higher current density.

The current density of thermionic emission can be calculated with the Richardson-Dushman equation [20]

$$j = A_0 T_{\mathrm{cath}}^2 e^{-\frac{W_\mathrm{A}}{k_\mathrm{B} T_{\mathrm{cath}}}}. \tag{3}$$

Here W_A is the work function, A_0 specifies the material constant of the cathode, the so called Richardson constant, and T_{cath} represents the temperature of the cathode. The work function of the material depends on the temperature. For a BTD of the type 411 M [20] it holds the dependency

$$W_\mathrm{A} = 1.43\,\mathrm{eV} + 0.000\,399\,\mathrm{eV\,K^{-1}} \cdot T_{\mathrm{cath}} \tag{4}$$

and the value of the Richardson constant $A_0 = 60 \times 10^4\,\mathrm{A\,K^{-2}\,m^{-2}}$ [21]. Typical operation temperatures of BTD lie between 1200–1400 K. We decided to use a temperature of 1300 K leading to a sufficient current density and emittance. Furthermore, a smaller temperature results in a longer lifetime of the cathode.

The emission properties of the cathode define the minimally reachable emittance. The normalized rms emittance of a cathode [22] can be calculated from

$$\epsilon = \sigma \sqrt{\frac{k_\mathrm{B} T_\mathrm{cath}}{m_0 c^2}}. \tag{5}$$

k_B denotes the Boltzmann constant, m_0 is the electron rest mass and c indicates the speed of light. The parameter σ represents the rms-dimension of the emitting area. To decrease the emittance, the size and the temperature can be decreased, whereas the size has a higher impact. Inserting the temperature of the BTD cathode $T_\mathrm{cath} = 1300\,\mathrm{K}$ into equation 5 gives an overall width of the cathode $y_\mathrm{cath} = 1.5\,\mathrm{mm}$ for achieving an emittance of $\epsilon_y = 0.17\,\mathrm{mm\,mrad}$.

2.6 Pierce electrode

The PE is an electrode with a conical shape to form the electric field to focus the beam after extraction. The reason is to counteract the repulsive space charge force of the beam, which is very large at low energies. The angle with respect to the cathode must be adapted to the used beam current. In addition, applying a negative potential to the PE is a fast possibility to shut down the beam.

2.7 Focusing magnet

The focusing of the electron beam can be achieved by a quadrupole magnet. The magnetic field focuses the beam in one dimension (here the y-dimension) and defocuses the beam in the perpendicular dimension. This is sufficient because the small focus is only demanded in one dimension. This magnet uses a high field gradient (excitation current $I_\mathrm{q2} = 1.2\,\mathrm{A}$) to strongly focus the beam. However, the focusing and defocusing are not independent of each other. Therefore, a second quadrupole magnet is needed. The tracking simulations showed that a first quadrupole magnet, which slightly focuses the beam in x-direction (excitation current $I_\mathrm{q1} = 0.1\,\mathrm{A}$), is required to achieve the demanded horizontal focal spot dimension. Furthermore, a second quadrupole magnet adds a degree of freedom to change the focal spot dimension in general. The positions of the

quadrupole magnets are limited by the other parts, such as anode and target. However, the goal was to construct a beamline as short as possible, because the aim was to construct a compact source. Furthermore, the space charge force acting on the beam along the beamline increases the emittance.

3 Results

3.1 Tracking simulations

Simulations were performed with round and rectangular cathodes, whereas only with a rectangular cathode the demanded parameters could be achieved. Furthermore, several geometries of the cathode and anode were simulated. The simulations showed that two quadrupole magnets are necessary to achieve appropriate beam dimensions in both directions in the focal plane and to have a sufficient number of degrees of freedom to compensate fabrication and alignment errors.

The most crucial parameter concerning the emittance of the vertical direction and therefore the minimal focal spot size is the vertical width of the cathode y_{cath}. A sufficient value for the horizontal cathode dimension is $x_{\mathrm{cath}} = 22\,\mathrm{mm}$. With this size of the cathode, the horizontal dimension of the electron beam stayed below 30 mm in the focal plane. When changing the vertical cathode width, the cathode temperature T_{cath} must also be changed to extract a constant current of $I_{\mathrm{cath}} = 300\,\mathrm{mA}$ (see equation 3). Figure 2 shows the influence of the vertical cathode width on the emittance $\epsilon_{y,\mathrm{rms}}$. According to equation (5), the emittance increased with increasing dimension of the cathode, which will not be compensated by the decreasing temperature. Therefore, y_{cath} must be as small as possible. To reach a sufficient emittance and focal spot size, the vertical width must be smaller than 0.5 mm. Fabrication tolerances and mechanical stability led to the decision to use a cathode width of $y_{\mathrm{cath}} = 0.4\,\mathrm{mm}$. The reason for the comparable emittances of widths 0.2 mm and 0.4 mm at the end of the beamline was that the used geometry and parameters were optimized

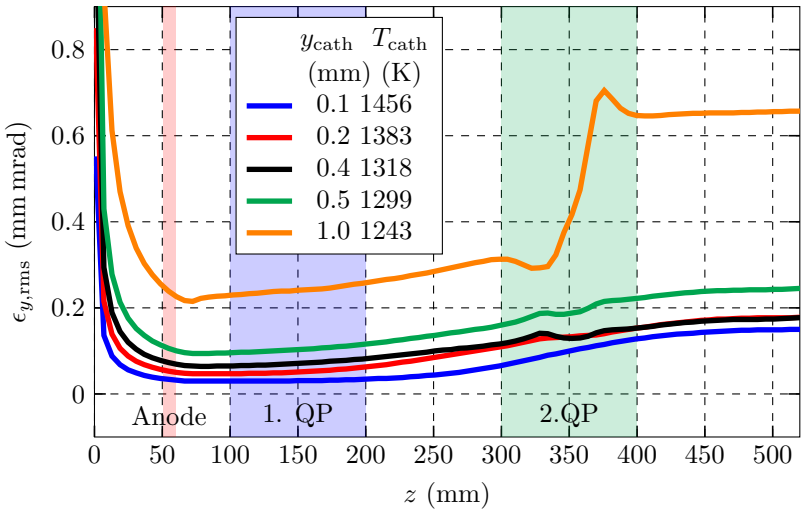

Figure 2: Vertical emittance along the beamline as a function of the width y_{cath}. For a constant current of 300 mA, the temperature of the cathode has to decrease when increasing the cathode width.

for $y_{\mathrm{cath}} = 0.4\,\mathrm{mm}$.

With a PE angle of $\alpha_{\mathrm{PE}} = 21.5°$, the lowest emittance behind the anode were achieved. Furthermore, the voltage that must be applied to the PE to stop the beam was specified. Figure 3 shows that an additional voltage of $\Delta U_{\mathrm{PE}} = -600\,\mathrm{V}$ with respect to the voltage of the cathode stops extraction of the beam.

3.2 Electrostatic simulations

Figure 4 shows the result for the final dimensions of the vacuum chamber and the cathode-PE assembly. The distance between cathode and anode was 67 mm and the radius of the PE was 35 mm. With this setup, the electric field strength between cathode, PE, anode and vacuum chamber stayed below $E < 10\,\mathrm{MV\,m^{-1}}$.

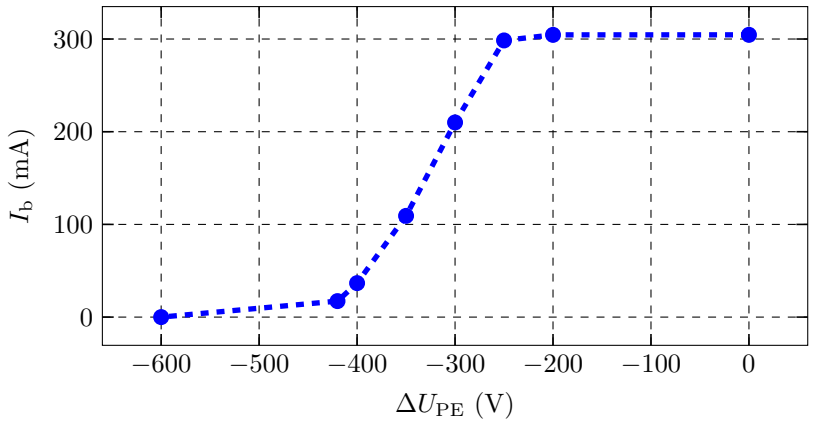

Figure 3: Beam current I_b as a function of the additionally applied PE voltage.

3.3 Thermal simulations

A change of the relative positions of the cathode and the PE was observed. Figure 5 shows the deformation in z-direction. In this model, the z-axis points towards the opposite direction of the beam. The equilibrium temperature of the cathode reached 1135 °C. The Pierce electrode warms up to 36.1 °C. The overall elongation in z-direction of the cathode and PE was simulated to -0.23 mm and -0.13 mm respectively. This results in a relative displacement of about $\Delta l = 0.1$ mm, which needs to be compensated with appropriate fabrication of the cathode-PE assembly.

3.4 Final design and focal beam spot

Figure 6 shows a half section of the CAD-model of the beamline. The distance between the rectangular cathode and the target is 488 mm. The PE and the flat anode are visible. Additional to the mentioned quadrupole magnets, a steerer magnet will be installed in the beamline. The steerer combines two dipole magnets in a perpendicular arrangement, each realized with air coils. They allow to adjust the vertical and horizontal position of the beam on the target. Due to the small distance between the target and the vacuum chamber, secondary

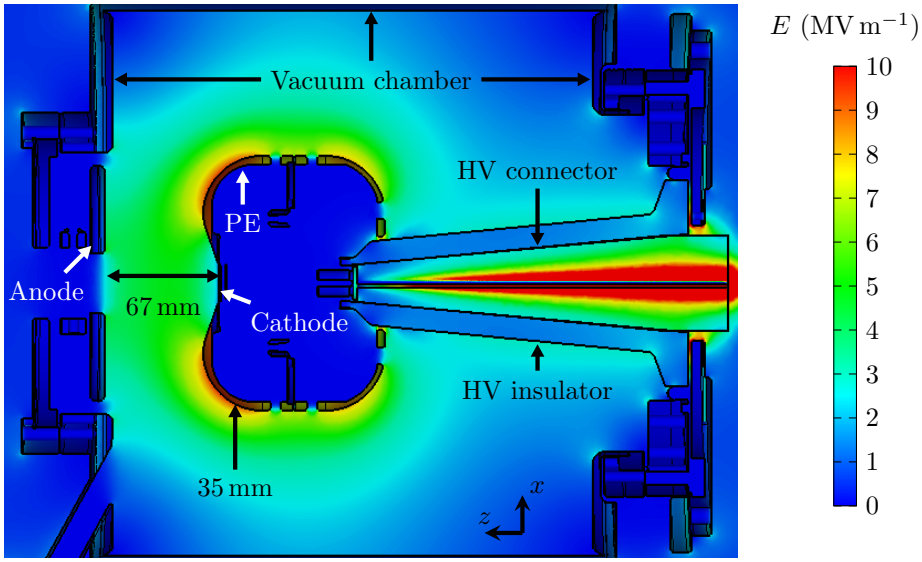

Figure 4: Electric field E between cathode, anode and vacuum chamber.

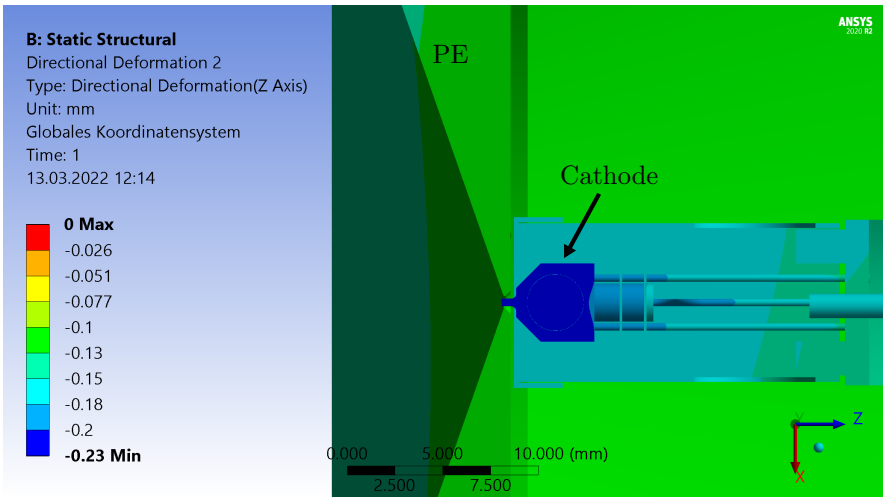

Figure 5: FEA results of the thermal simulation showing directional deformation with regard to the z-axis.

electrons will cause a rise in temperature of the vacuum chamber to 690 °C. For this reason, a cooling system will be integrated into the vacuum chamber and

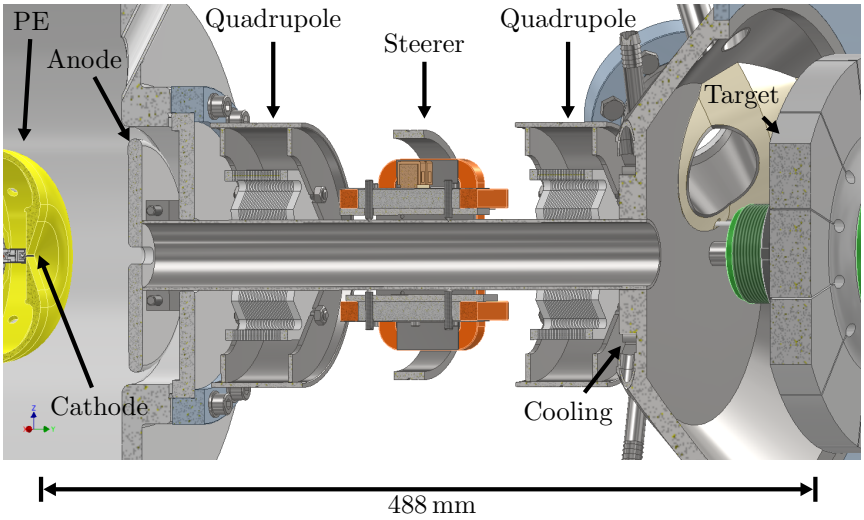

Figure 6: Half section view of the electron source, beamline, and target.

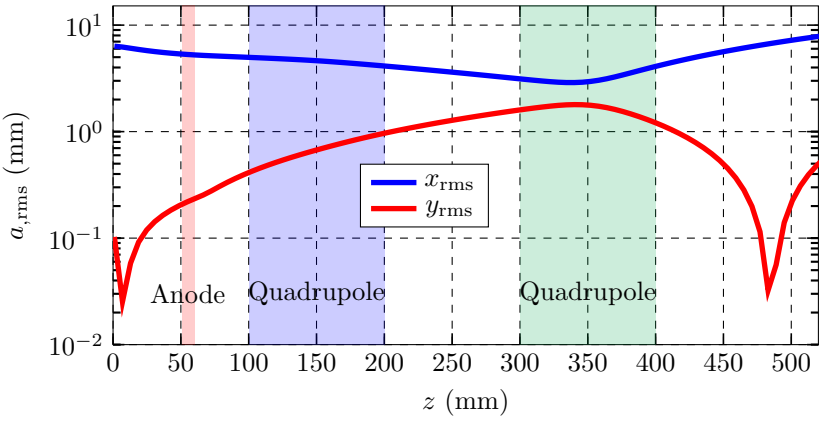

Figure 7: Beam dimensions x_{rms} and y_{rms} along the beamline.

limits the rise of temperature to 250 °C. The values were obtained by thermal simulations. In Figure 7, the beam dimensions x_{rms} and y_{rms} along the beamline are recognizable. In front of the anode, the focusing of the PE is visible. The first quadrupole magnet with an excitation current of $I_{\mathrm{q1}} = 0.1\,\mathrm{A}$ weakly focuses the beam in the x-direction to achieve a focal spot smaller than $x_{\mathrm{f}} < 30\,\mathrm{mm}$ in the horizontal direction. Simultaneously, it defocuses the beam in vertical direction

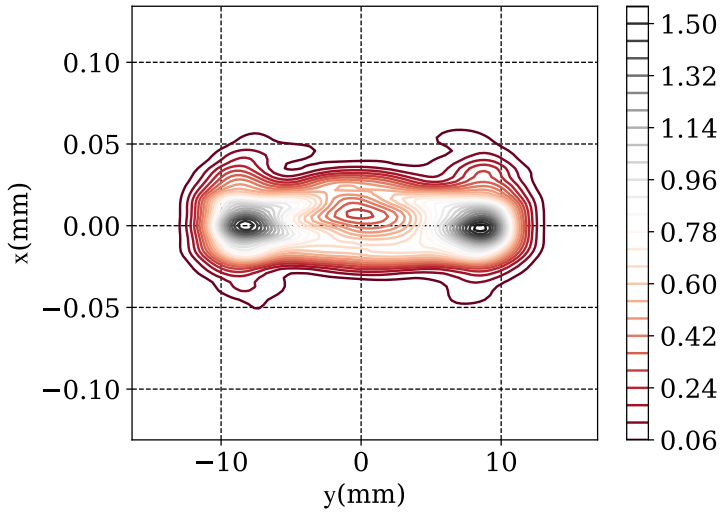

Figure 8: Focal beam spot with the final setup of the electron gun and beamline.

to get a larger beam dimension at the second quadrupole magnet resulting in a stronger focusing in this dimension. The second quadrupole magnet with an excitation current of $I_{q2} = 1.2\,\mathrm{A}$ then strongly focuses beam in the y-direction leading to a vertical focal beam size $y_f = 50\,\mu\mathrm{m}$. The focus appears at a distance of $z = 488\,\mathrm{mm}$, corresponding to the position of the target.

Fig. 8 depicts the electron intensity distribution at the target with the final setup of the electron gun and beamline in arbitrary units. Most of the electrons hit the target within spot dimensions of $0.05 \times 22\,\mathrm{mm}$, which is a satisfying result. However, an inhomogeneous distribution can be observed. Especially in the horizontal direction, two maxima in intensity are recognizable. They appear around 9 mm off center. Here, the intensity is about a factor of 2 higher than in the center of the beam.

4 Discussion

The LFxT seems to be a promising candidate for realizing a compact microbeam source for clinical application. To match the requests of the LFxT, a dedicated

electron source and beamline have to be developed. The high beam current in combination with the small focal spot and the compact construction are challenging demands.

For the prototype of the LFxT, we decided to use a thermal cathode to deliver the beam current of $I_\mathrm{b} = 0.3\,\mathrm{A}$ due to a higher robustness compared to photo cathodes. Nevertheless, more robust photo cathodes are under development and could be an option for a clinical device with short beam times as they might achieve a smaller initial emittance than thermal cathodes. As a thermal cathode, a barium tungsten dispenser cathode was chosen because it can deliver sufficient current densities and at the same time has lower demands on the vacuum quality than hexaboride cathodes. However, for the clinical device hexaborid cathodes with their higher current densities must be considered.

To realize the small focal spot in one dimension, the emittance of the beam in this dimension must be smaller than $\epsilon_y = 0.17\,\mathrm{mm\,mrad}$. To achieve this and at the same time deliver the high beam current, using a rectangular cathode is mandatory. Even if using other cathode types for the clinical device the necessity of working with a rectangular cathode will not change. With a cathode width of $y_\mathrm{cath} = 0.4\,\mathrm{mm}$, the simulations resulted in emittances of the needed order of magnitude, and the demanded focal spot width $y_\mathrm{f} = 50\,\mathrm{\mu m}$ could be reached. Due to emittance growth caused by the quadrupole magnets and the space charge, the cathode width must be smaller than calculated with equation 5. Admittedly, creating smaller focal spot widths is very difficult. Therefore, achieving the same focal spot with higher currents asks for other cathodes types with a higher current density. Additionally, with higher current densities, it could be possible to decrease the horizontal dimension of the cathode. A cathode with a large aspect ratio is more difficult to fabricate within tight tolerances and additionally, a smaller aspect ratio will improve the homogeneity of the focal spot.

The PE will supply sufficient focusing of the beam after extraction of the cathode, to compensate increase of the beam dimension caused by space charge. Furthermore, applying an additional voltage of $\Delta U_\mathrm{PE} = -600\,\mathrm{V}$ to the PE will

shut down the beam. The reason for this relatively low voltage compared to the accelerating voltage is the small width of the cathode as even a small voltage leads to a adequately high electric field shielding the accelerating field. So, there is no need to install a mechanical shutter to stop the x-ray beam.

The tracking simulations showed that using two quadrupole magnets is essential to achieve both demanded focal spot dimensions and to be more flexible to react to fabrication errors. A steerer magnet will be installed enabling positioning of the focal spot. However, every magnetic field has stray fields, which means that non-linear portions lead to an emittance growth and therefore must be as low as possible.

The electrostatic simulations helped to find adequate shapes and distances of the components. The goal to stay below electric field strengths of $E < 10\,\mathrm{MV\,m^{-1}}$ was achieved. A higher accelerating voltage of the clinical device makes larger distances between the components and larger radii obligatory to reach the same field strengths. With a new insulator design, operation with an acceleration voltage of 600 kV should be feasible. An inspiring example is the source in [23], where a stable operation with a voltage of 500 kV was demonstrated. However, the larger beam current used at the clinical apparatus could make higher field strengths necessary. Furthermore, it has to be mentioned that both photon energy and photon fluence are important for clinical applications. For that reason, a further increase of acceleration voltage can be considered to achieve a larger penetration depth. The experience gained with the prototype will merge into the development of the clinical device.

The thermal simulations showed a small longitudinal displacement of $\Delta l = 0.1\,\mathrm{mm}$ between the cathode and PE respectively. The cathode-PE assembly manufacturing has to be designed in regard to this difference. Furthermore, in the construction very thin shims are foreseen to be able to compensate deviations from the simulation and manufacturing tolerances.

The two maxima in the particle distribution in the focal plane were a result of the strongly eccentric cathode. Along the x-direction, only particles at the edge of the cathode were focused by the PE. Particles from the center of the cathode

with transverse momentum will move to the rim of the beam, where they also were focused. This happened directly after extraction of the electrons with a low longitudinal energy and formed the observed pattern, which will then exist along the entire beamline. Nevertheless, the focal spot size of $0.05 \times 22\,\mathrm{mm}$ satisfied the requirements. Additional Monte Carlo simulations using this non-uniform electron beam phase space for x-ray production at a tungsten target demonstrated that the microbeam dose distribution did not markedly differ from a homogeneous electron beam of the same size. With a filtration of 1 mm aluminum, the microbeam dose distribution showed a sharp peak-valley profile and a PVDR above 15 throughout a 100 mm-thick water phantom at a distance of 21 cm from the focal spot. The PVDR was slightly lower than presented in [8] because of the lower mean energy due to less filtration. The simulated dose rate was $10\,\mathrm{Gy\,s^{-1}}$ at a water depth of 15 mm. These simulations validated the suitability of the electron beam for MRT at high dose rates. However, the inhomogeneous electron distribution leads to a higher maximum temperature at the target compared to a homogeneous focal spot, which must be considered.
In this work, we focused mainly on the generation of microbeams for radiation oncology. However, beyond the generation of microbeams, the special properties of the LFxT render it suitable for other applications. One example is ultra-high dose rate radiation therapy (FLASH). So far, most FLASH treatments were performed at modified linear accelerators with electron beams. The LFxT may allow FLASH treatments with orthovoltage x-rays, with substantially improved dose distributions compared to MeV electrons. Apart applications in imaging are conceivable. Phase contrast imaging and virtual histology may benefit from the small source size and spatial coherence in one spatial dimension [24]. Applications in x-ray fluorescence imaging may also be feasible [25].

5 Conclusions

The simulations demonstrated the feasibility of an electron source and beamline to provide a strongly eccentric focal spot with a size of $0.05 \times 20\,\mathrm{mm^2}$ with a

beam current of 0.3 A. The beam energy of 300 keV was achieved with an electric field below 10 MV m^{-1}. The prototype of the LFxT and its periphery is under construction at the moment. The prototype will deliver valuable insights and results concerning the development of an electron source for a clinical device with a beam energy of 600 keV. Especially, a different cathode material must be considered to provide a higher current with a comparable emittance and to produce a more homogeneous electron distribution. Furthermore, higher acceleration gradients could be advantageous concerning space charge effects. Also, an adjustment of the PE could be necessary. At last, the magnet design must be applied to the higher energy. In addition, biological and biological preclinical experiments conducted with the prototype will evaluate the potential of the LFxT as a compact source for clinical MRT.

Conflict of interest statement

The authors have no conflict of interest to declare.

Acknowledgments

This work was supported by the German Research Foundation (Deutsche Forschungsgemeinschaft) through the Emmy Noether Programme with grant number 416790481 and the research grant 389238549.

References

[1] Slatkin DN, Spanne PO, Dilmanian FA, and Sandbora M. Microbeam radiation therapy. Medical Physics 1992; 19(6):1395–1400. https://doi.org/10.1118/1.596771.

[2] Bouchet A, Bräuer E, Prezado Y, El Atifi M, Rogalev L, Le Clec'h C, et al. Better Efficacy of Synchrotron Spatially Microfractionated Radiation Therapy Than Uniform Radiation Therapy on Glioma. Interna-

tional Journal of Radiation Oncology Biology Physics 2016; 95(5):1485–94. https://doi.org/10.1016/j.ijrobp.2016.03.040.

[3] Smyth LML, Donoghue JF, Ventura JA, Livingstone J, Bailey T, Day LRJ, et al. Comparative toxicity of synchrotron and conventional radiation therapy based on total and partial body irradiation in a murine model. Scientific Reports 2018; 8(1):1–11. https://doi.org/10.1038/s41598-018-30543-1.

[4] Mohiuddin M, Fujita M, Regine WF, Megooni AS, Ibbott GS, and Ahmed MM. High-dose spatially-fractionated radiation (GRID): A new paradigm in the management of advanced cancers. International Journal of Radiation Oncology Biology Physics 1999; 45(3):721–7. https://doi.org/10.1016/S0360-3016(99)00170-4.

[5] Schneider T. Technical aspects of proton minibeam radiation therapy: Minibeam generation and delivery. Physica Medica 2022; 100:64–71. ISSN 1120-1797. https://doi.org/10.1016/j.ejmp.2022.06.010.

[6] Bartzsch S, Corde S, Crosbie JC, Day LRJ, Donzelli M, Krisch M, et al. Technical advances in X-ray microbeam radiation therapy. Physics in Medicine and Biology 2020; 65(2):02TR01. https://doi.org/10.1088/1361-6560/ab5507.

[7] Bartzsch S and Oelfke U. Line focus x-ray tubes—a new concept to produce high brilliance x-rays. Physics in Medicine & Biology 2017; 62(22):8600–15. https://doi.org/10.1088/1361-6560/aa910b.

[8] Winter J, Galek M, Matejcek C, Wilkens JJ, Aulenbacher K, Combs SE, and Bartzsch S. Clinical microbeam radiation therapy with a compact source: specifications of the line-focus x-ray tube. Physics and Imaging in Radiation Oncology 2020; 14:74–81.

[9] Kraus KM, Winter J, Zhang Y, Ahmed M, Combs SE, Wilkens JJ, and Bartzsch S. Treatment planning study for microbeam radiotherapy using

clinical patient data. Cancers 2022; 14(3). ISSN 2072-6694. https://doi.org/10.3390/cancers14030685.

[10] Ringler R. Physikalisch-Technische Grundlagen der Röntgendiagnostik. In: Schlegel W, Karger CP, Jäkel O, editors. Medizinische Physik. Berlin, Heidelberg: Springer Spektrum; 2018, p. 123–138. https://doi.org/10.1007/978-3-662-54801-1_6.

[11] Wille K. Physik der Teilchenbeschleuniger und Synchrotronstrahlungsquellen. Stuttgart: B. G. Teubner; 1996.

[12] Matejcek C. Strahldynamik der Niederenergie-Strahlfürung von MESA unter Berücksichtigung von Raumladung und Multipol-Beiträgen höherer Ordnung. PhD thesis Johannes Gutenberg-Universität Mainz 2021.

[13] Wangler TP. RF linear accelerators. Weinheim: WILEY-VCH; 2008.

[14] Technology Computer Simulation. CST Studio Suite. `http://www.cst.com/` 2018. Aachen, Deutschland.

[15] Sinclair CK, Dylla H, Siggins TL, Manos D, Wu L, and Venhaus TJ. Dramatic reduction of dc field emission from large area electrodes by plasma-source ion implantation. In *Particle Accelerator Conference, 2001. PAC 2001. Proceedings of the 2001* pages 610 – 612 vol.1 02 2001;. https://doi.org/10.1109/PAC.2001.987582.

[16] Giere S, Kurrat M, and Schumann U. Hv dielectric strength of shielding electrodes in vacuum circuit-breakers. In *20th International Symposium on Discharges and Electrical Insulation in Vacuum* pages 119–122 2002;. https://doi.org/10.1109/ISDEIV.2002.1027323.

[17] Ansys Inc. Ansys mechanical (version 2020 r2). `https://www.ansys.com/` 2020. Pennsylvania, USA.

[18] Schalles M. Berechnung des effektiven emissionsgrades von referenzstrahlen aus aluminiumoxid. In *16. GMA/ITG-Fachtagung Sensoren und Messsysteme 2012* 2012;. https://doi.org/10.5162/sensoren2012/1.3.2.

[19] Limited Omega Engineering. Emissivity of common materials. https://www.omega.co.uk/literature/transactions/volume1/emissivitya.html#g. [accessed 8 Juni 2021].

[20] Cronin JL. Modern dispenser cathodes. In *IEE Proceedings / Solid State and Electron Devices* volume 128 pages 19–32 February 1981;. https://doi.org/10.1049/ip-i-1.1981.0012.

[21] De DK and Olawole OC. Modification of richardson-dushman therminonic emission current density equation for nano-materials. In *3rd International Conference on African Development Issues (CU-ICADI 2016)* August 2016;. URL https://www.researchgate.net/publication/304393398_Modifications_of_Richardson-Dushman_Thermionic_Emission_Current_Density_Equation_for_Nano-_Materials.

[22] Bazarov IV et al. Thermal emittance and response time measurements of negative electron affinity photocathodes. Journal of Applied Physics 2008; (103).

[23] Nishimori N, Nagai R, Hajima R, Yamamoto M, Honda Y, Miyajima T, and Uchiyama T. Operational experience of a 500 kv photoemission gun. Phys. Rev. Accel. Beams May 2019; 22:053402. https://doi.org/10.1103/PhysRevAccelBeams.22.053402.

[24] Vassholz M, Koberstein-Schwarz B, Ruhlandt A, Krenkel M, and Salditt T. New x-ray tomography method based on the 3d radon transform compatible with anisotropic sources. Physical Review Letters 2016; 116(8):088101.

[25] Grüner F, Blumendorf F, Schmutzler O, Staufer T, Bradbury M, Wiesner U, Rosentreter T, Loers G, Lutz D, Richter B, et al. Localising functionalised gold-nanoparticles in murine spinal cords by x-ray fluorescence imaging and background-reduction through spatial filtering for human-sized objects. Scientific reports 2018; 8(1):1–12.